J. Fluid Mech. (1975), *vol.* 69, *part* 1, *pp.* 27–40
Printed in Great Britain

The 'sliced-cylinder' laboratory model of the wind-driven ocean circulation. Part 1. Steady forcing and topographic Rossby wave instability

By R. C. BEARDSLEY AND K. ROBBINS
Department of Meteorology, Massachusetts Institute of Technology, Cambridge

(Received 7 March 1974)

The nonlinear response of the 'sliced-cylinder' laboratory model for the wind-driven ocean circulation is re-examined here in part 1 for the case of strong steady forcing. Introduced by Pedlosky & Greenspan (1967), the model consists of a rapidly rotating right cylinder with a planar sloping bottom. The homogeneous contained fluid is driven by the slow rotation of the flat upper lid relative to the rest of the basin. Except in thin Ekman and Stewartson boundary layers on the solid surfaces of the basin, the horizontal flow in the interior and western boundary layer is constrained by the rapid rotation of the basin to be independent of depth. The model thus effectively simulates geophysical flows through the physical analogy between topographic vortex stretching in the laboratory model and the creation of relative vorticity in planetary flows by the β effect.

As the forcing is increased, the flow in both the sliced-cylinder laboratory and numerical models first exhibits downstream intensification in the western boundary layer. At greater forcing, separation of the western boundary current occurs with the development of stationary topographic Rossby waves in the western boundary-layer transition regions. The observed flow ultimately becomes unstable when a critical Ekman-layer Reynolds number is exceeded. We first review and compare the experimental and numerical descriptions of this low-frequency instability, then present a simple theoretical model which successfully explains this observed instability in terms of the *local* breakdown of the finite-amplitude topographic Rossby waves embedded in the western boundary current transition region. The inviscid stability analysis of Lorenz (1972) is extended to include viscous effects, with the consequence that dissipative processes in the sliced-cylinder problem (i.e. lateral and bottom friction) are shown to inhibit the onset of the instability until the topographic Rossby wave slope exceeds a finite critical value.

1. Introduction

The wind-driven ocean circulation problem has been studied widely in the past two and a half decades since the pioneering work of Sverdrup (1947), who pointed out the interior vorticity balance between the advection of planetary

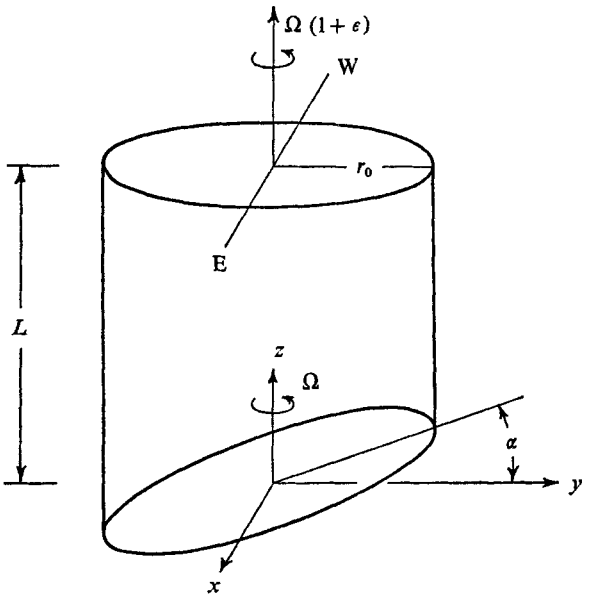

FIGURE 1. The 'sliced-cylinder' geometry.

vorticity and the curl of the surface wind stress, and Stommel (1948), who discovered the theoretical basis for western intensification of boundary currents. From their work, a hierarchy of more sophisticated and realistic models has evolved, with recent interest focusing on the more complicated transient circulations generated by low-frequency time-dependent wind stresses. A number of different laboratory models have concurrently been developed to isolate and illustrate the more important features of the wind-driven ocean circulation (see Greenspan 1968, § 5.3).

Our interest will concentrate on the 'sliced-cylinder' laboratory model introduced by Pedlosky & Greenspan (1967). This model consists of a rapidly rotating cylindrical basin with a planar sloping bottom filled with a viscous homogeneous fluid (see figure 1). The surface wind stress is simulated by a viscous stress caused by the slow rotation of the flat upper lid relative to the rest of the basin. Except in thin Ekman and Stewartson boundary layers on the solid surfaces of the basin, the horizontal velocity field is constrained by the rapid rotation of the basin to be independent of depth along the rotation axis (a consequence of the Taylor–Proudman theorem). The sliced-cylinder model effectively simulates planetary flows, since vortex stretching in the interior and western boundary current by flow across the sloping bottom is directly analogous to the creation of relative vorticity in large-scale oceanic flows by the northward increase in horizontal Coriolis acceleration (the β effect).

The response of the sliced-cylinder model to a steady wind stress depends critically on the ratio of the total depth variation to the Ekman-layer thickness (see Beardsley 1969). The key external non-dimensional parameters governing the flow in the laboratory model are (i) the Ekman number $E = \nu/\Omega L^2$ (ν is the kinematic viscosity of the fluid, Ω is the angular velocity of the basin, and L is

the average depth); (ii) the Rossby number ϵ (which is the relative angular velocity of the driving lid scaled by Ω); and (iii) the bottom slope $\tan\alpha$ (see figure 1).

The aspect ratio r_0/L is assumed to be unity, to correspond to the laboratory experiments. When the applied stress is small ($\epsilon \lesssim E^{\frac{1}{2}}$) and the total depth variation less than the thickness of the Ekman layer (i.e. $\tan\alpha \ll E^{\frac{1}{2}} \ll 1$), the interior flow does not feel the topography, and remains essentially axisymmetric. When the bottom slope slightly exceeds the scaled Ekman-layer thickness

$$(E^{\frac{1}{2}} \ll \tan\alpha \ll E^{\frac{1}{4}}),$$

the interior flow exhibits a broad western boundary current, in which the orographic vortex stretching is balanced by Ekman-layer suction. The interior dynamics are identical in this parameter range with Stommel's (1948) model for two-dimensional β-plane flow with 'bottom' friction. For larger bottom slopes in the range $E^{\frac{1}{4}} \ll \tan\alpha \ll 1$, the stronger orographic vortex stretching in the western boundary current becomes primarily balanced by the lateral diffusion of vorticity. Thus the dynamics in the interior and western boundary layer become identical to lowest order with Munk's (1950) β-plane model with lateral friction.

A detailed experimental investigation of the sliced-cylinder model has been conducted in the Munk regime (i.e. $E^{\frac{1}{4}} \ll \tan\alpha < 1$), and the results reported in Beardsley (1969). While many features of the linear analysis were confirmed by these experiments, many questions remained concerning the nonlinear behaviour of the model in response to large steady wind stresses. As the applied stress is increased, the flow first exhibits downstream intensification in the western boundary current, due to the increased importance of inertia in the local momentum balance in the boundary layer. Separation of the western boundary current occurs at greater stresses; and ultimately the observed laboratory flow becomes unstable when the Ekman-layer Reynolds number exceeds a critical value. While the key external parameters governing the onset of this low-frequency instability have been determined, the dynamical cause has not yet been explained.

Beardsley (1973*a*, *b*) made two attempts to study the nonlinear behaviour of the sliced-cylinder laboratory model, using two-dimensional numerical models. The first model involved a re-examination of the vorticity equation for two-dimensional flow on a β plane with lateral friction (as studied by Bryan 1963), but now for the case of a circular basin. While the numerical solutions exhibited separation of the western boundary layer with increasing wind stress, the numerical model failed to simulate closely the observed flow in the laboratory model. The principal cause of this failure was the omission of direct Ekman-layer suction in the governing vorticity equation. Analysis by Beardsley (1973*a*) showed that direct Ekman-layer suction plays an important role in the vorticity balance in the *transition* regions between the interior, where the Sverdrup balance prevails, and the high-velocity core of the western boundary layer, where the Munk balance with lateral friction dominates. Thus the dynamics of the first numerical model were approximately analogous to the laboratory model in most but not all, of the basin, especially the northern transition region.

The second numerical model developed incorporated direct Ekman-layer suction in the governing two-dimensional vorticity equation. An extremely efficient numerical scheme has been developed using Israeli's (1970) implicit technique to solve the finite-difference equations on a polar grid net with non-uniform radial spacing, for good boundary-layer resolution. We have now used this numerical model to study the analogue response of the sliced-cylinder model to both steady and oscillatory wind forcing. The results for a steady wind forcing and a complete description of the numerical model have been presented by Beardsley (1973*b*). In this paper we summarize the experimental and numerical description of the low-frequency flow instability observed in the downstream transition region of the nonlinear western boundary current. Then we present a theoretical model which explains this instability in terms of the local breakdown of a finite-amplitude topographic Rossby wave embedded in the western boundary current transition flow. The results of the laboratory and numerical experiments for an oscillatory wind forcing will be presented in the following paper. For completeness, we begin with a brief derivation of the governing vorticity equation used in both numerical studies.

2. Derivation of model vorticity equation

A two-dimensional vorticity equation was derived for the sliced-cylinder model in a consistent manner by Greenspan (1969). This derivation is based on a perturbation expansion with the bottom slope being the small parameter. It is repeated here for completeness, and to illustrate the scaling used in the two models.

The appropriate non-dimensional momentum and continuity equations for a rotating homogeneous viscous fluid are

$$2s\left(\frac{\partial \mathbf{q}}{\partial \tau}\right)+\epsilon\mathbf{q}\,.\,\nabla\mathbf{q}+2\hat{\mathbf{k}}\times\mathbf{q}=-\nabla p+E\nabla^2\mathbf{q},\quad \nabla\,.\,\mathbf{q}=0, \tag{1}$$

where the length, time and velocity variables have been scaled by L, $(2s\Omega)^{-1}$ and $\epsilon\Omega L$ respectively, with the bottom slope $s\equiv\tan\alpha$ assumed to be small. E and ϵ are the Ekman and external Rossby numbers for the laboratory model. (In the experiments to be described here, these parameters have typical values of $s=0{\cdot}178$, $1\leqslant E\times 10^5\leqslant 5$, $0{\cdot}002<\epsilon<0{\cdot}14$.) We shall rescale $\epsilon=sR$ and break the viscous term into horizontal and vertical components, i.e.

$$E\nabla^2=sE_h\nabla_h^2+s^2E_v\,\partial^2/\partial z^2.$$

Substitution of these expressions into the momentum equation yields

$$s\left(2\frac{\partial \mathbf{q}}{\partial \tau}+R\mathbf{q}\,.\,\nabla\mathbf{q}\right)+2\hat{\mathbf{k}}\times\mathbf{q}=-\nabla p+s\left(E_h\nabla_h\mathbf{q}^2+sE_v\frac{\partial^2}{\partial z^2}\mathbf{q}\right). \tag{2}$$

The no-slip boundary conditions are $\mathbf{q}=0$ at $r=a$ and $z=sy$, and $\mathbf{q}=r\hat{\boldsymbol{\theta}}$ at $z=1$.

The velocity and pressure are now written as perturbation expansions in s of the form

$$\mathbf{q}=\mathbf{q}_0+s\mathbf{q}_1+\ldots,\quad p=p_0+sp_1+\ldots. \tag{3}$$

The substitution of these series into the basic equations and boundary conditions yields an infinite sequence of problems for the unknown functions. Greenspan has shown that a governing equation for $\mathbf{q}_0$ arises from the solution to the first-order problem.

The flow to lowest order in s is geostrophic,

$$2\hat{\mathbf{k}} \times \mathbf{q}_0 = -\nabla p_0, \quad \nabla . \mathbf{q}_0 = 0. \tag{4}$$

Thus it satisfies the Taylor–Proudman theorem

$$\partial \mathbf{q}_0 / \partial z = 0. \tag{5}$$

The flow in the sliced-cylinder laboratory model is mechanically driven by the relative rotation of the upper lid. The resulting Ekman boundary layers on the top and bottom surfaces may be analysed separately (see Greenspan 1968). We use here the equivalent steady Ekman-layer compatibility condition between the vertical velocity into the Ekman layer and the boundary and interior velocity fields, which yield

$$\hat{\mathbf{k}} . \mathbf{q}_1 = \tfrac{1}{2} E_v^{\frac{1}{2}} (+2 - \zeta_0) \quad \text{at} \quad z = 1, \tag{6a}$$

$$\hat{\mathbf{k}} . \mathbf{q}_1 = \hat{\mathbf{j}} . \mathbf{q}_0 + \tfrac{1}{2} E_v^{\frac{1}{2}} \zeta_0 \quad \text{at} \quad z = 0, \tag{6b}$$

where $\zeta_0 = \hat{\mathbf{k}} . \nabla \times \mathbf{q}_0$. Since $\mathbf{q}_0 . \hat{\mathbf{k}}$ vanishes identically, $\mathbf{q}_0$ must be a horizontal vector field independent of z. Thus a stream function ψ_0 exists for $\mathbf{q}_0$, and the lowest-order vorticity field is given by $\zeta_0 = \nabla^2 \psi_0$.

The first-order problem in s is

$$2\frac{\partial \mathbf{q}_0}{\partial \tau} + R\mathbf{q}_0 . \nabla \mathbf{q}_0 + 2\hat{\mathbf{k}} \times \mathbf{q}_1 = -\nabla p_1 + E_h \nabla_h^2 \mathbf{q}_0, \quad \nabla . \mathbf{q}_1 = 0. \tag{7}$$

The curl of the momentum equation (7) yields

$$2\frac{\partial \mathbf{q}_1}{\partial z} = \nabla \times \left\{ 2\frac{\partial \mathbf{q}_0}{\partial \tau} + R\mathbf{q}_0 . \nabla \mathbf{q}_0 - E_h \nabla_h^2 \mathbf{q}_0 \right\},$$

which may be integrated directly to give

$$\mathbf{q}_1 = \frac{z}{2} \nabla \times \left\{ 2\frac{\partial \mathbf{q}_0}{\partial \tau} + R\mathbf{q}_0 . \nabla \mathbf{q}_0 - E_h \nabla_h^2 \mathbf{q}_0 \right\} + \mathbf{A}(x, k, t).$$

The unknown vector function $\mathbf{A}$ is easily determined, using the lower Ekman-layer compatibility condition (6b) at $z = 0$,

$$\mathbf{A} . \hat{\mathbf{k}} = \hat{\mathbf{j}} . \mathbf{q}_0 + \tfrac{1}{2} E_v^{\frac{1}{2}} \zeta_0.$$

Elimination of $\mathbf{A}$, and use of the upper Ekman-layer condition (6a) at $z = 1$, results in the governing vorticity equation for the lowest-order velocity field:

$$2\frac{\partial \zeta_0}{\partial \tau} + R\mathbf{q}_0 . \nabla \zeta_0 + 2\hat{\mathbf{j}} . \mathbf{q}_0 = -2E_v^{\frac{1}{2}} \zeta_0 + E_h \nabla^2 \zeta_0 - E_v^{\frac{1}{2}} 2.$$

We now use the interior Sverdrup balance $\hat{\mathbf{j}} . \mathbf{q}_0 = E_v^{\frac{1}{2}}$ to rescale the stream-function and velocity fields, so that the final non-dimensional vorticity equation is

$$\partial \zeta / \partial \tau + R_0 \mathbf{u} . \nabla \zeta + \psi_x = -\delta \zeta + \hat{E} \nabla_h^2 \zeta - 1. \tag{8}$$

The two-dimensional velocity and vorticity fields are related through the stream function, $\mathbf{u} = \hat{\mathbf{k}} \times \nabla\psi$ and $\zeta = \nabla^2\psi$, with the velocity satisfying the no-slip condition at the basin boundary at $r = 1$. The new Rossby number and lateral and 'bottom' friction parameters in (8) are related to the laboratory parameters by

$$R_0 \equiv \frac{\epsilon E^{\frac{1}{2}}}{2s^2}, \quad \hat{E} \equiv \frac{E}{2s}, \quad \delta \equiv \frac{E^{\frac{1}{2}}}{s}. \tag{9}$$

As previously mentioned, numerical solutions to the finite-difference analogue of the vorticity equation (8) have been obtained, using a fast implicit method developed by Israeli (1970) for time-dependent viscous flow problems in plane or axisymmetric geometries. Israeli first analysed the iterative method developed by Pearson (1965). He found that a single optimum iteration parameter exists, and that it may be accurately estimated when the fluid is only slightly viscous (i.e. when $\nu\Delta t/L^2 \ll 1$, where ν is the fluid viscosity, Δt is the time increment, and L is a characteristic interior length scale). Israeli (see Orszag & Israeli 1972) then developed a direct method of computing the optimum iteration parameter which (in the case of the sliced-cylinder problem) gives overall convergence of the numerical scheme in one to two iterations per time step on the average, even in the more nonlinear regime with relatively large time-step increments.

The application of this method to the integration of the sliced-cylinder vorticity equation (8) considered here is straightforward (Beardsley 1973*b* discusses it in detail). The implicit scheme has been used to generate a number of numerical solutions. The ranges of the parameters R_0, $\hat{E}$ and δ, which govern the numerical model, have been chosen to correspond to the general parameter range explored earlier in the published sliced-cylinder laboratory experiments. Since direct Ekman-layer suction is included in the governing vorticity equation, the numerical model quickly reaches its steady state in several spin-up time periods (we here call δ^{-1} the non-dimensional spin-up time scale). The total kinetic energy of the system and the variability of ψ were examined to determine the steadiness of the flow.

3. Experiments in the nonlinear regime

Our interest here lies in a comparison of the laboratory and numerical experiments conducted in the nonlinear regime. As noted in Beardsley (1973*b*), the numerically generated stream function shows excellent agreement with the horizontal structure of the flow field measured in the laboratory model using streak photography. As the external Rossby number $|\epsilon|$ is increased past $E^{\frac{1}{2}}$, the western boundary current is first intensified downstream of $\theta = \pi$. When $|\epsilon| \simeq 3E^{\frac{1}{2}}$, the western boundary current separates from the wall and partially closes to form a vortex which intensifies and shifts downstream as $|\epsilon|$ is further increased. For $|\epsilon| \simeq 6E^{\frac{1}{2}}$, the centre of this vortex nears $\theta = 128°$, and moves systematically away from the side wall as the driving increases. In the transition region between the western boundary layer and the interior, stationary damped topographic Rossby waves appear, their amplitude and wavelength increasing with increasing $|\epsilon|$. This sequence of flow dependence on $|\epsilon|/E^{\frac{1}{2}}$ is clearly illu-

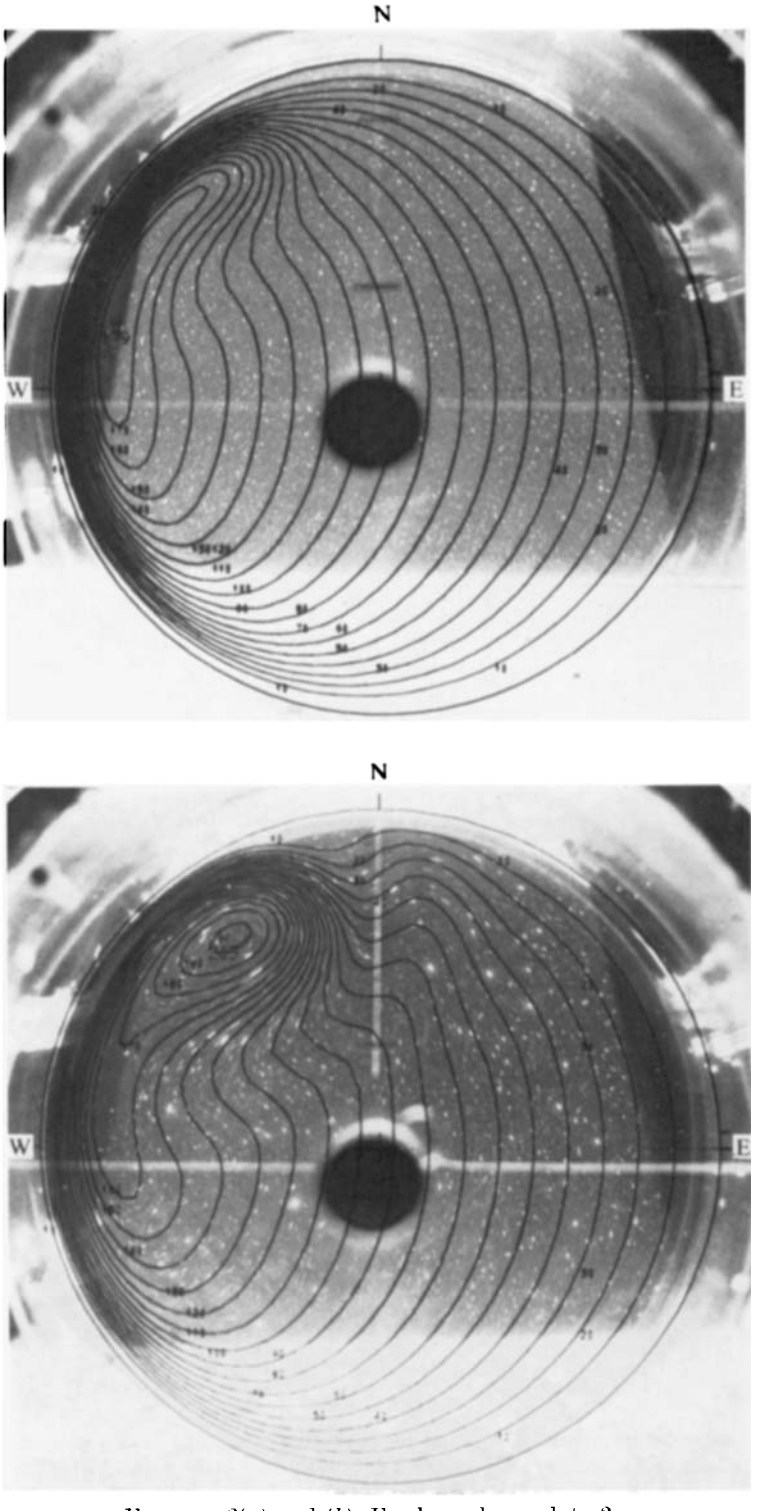

FIGURES 2(*a*) and (*b*). For legend see plate 2.

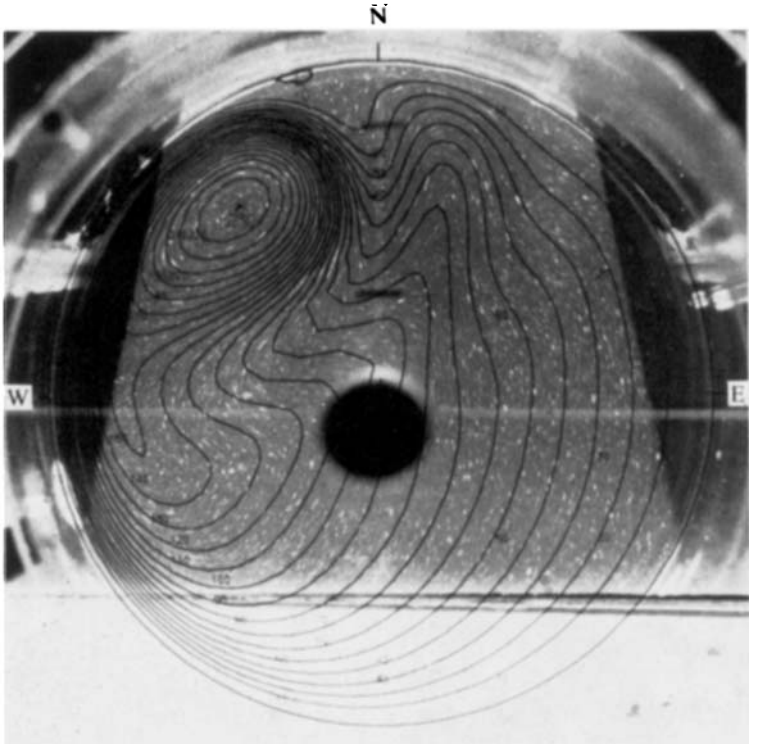

FIGURE 2. Composite figure showing numerical stream-function solutions superimposed on laboratory streak photographs for identical external parameters. Horizontal streak photographs were made at a mean depth of $z/L = 0{\cdot}43$ near the midplane of the basin. Laboratory parameter values are $\tan\alpha = 0{\cdot}178$, $E = 2{\cdot}03 \times 10^{-5}$. ϵ: (*a*) 0·019, (*b*) 0·038, (*c*) 0·0536.

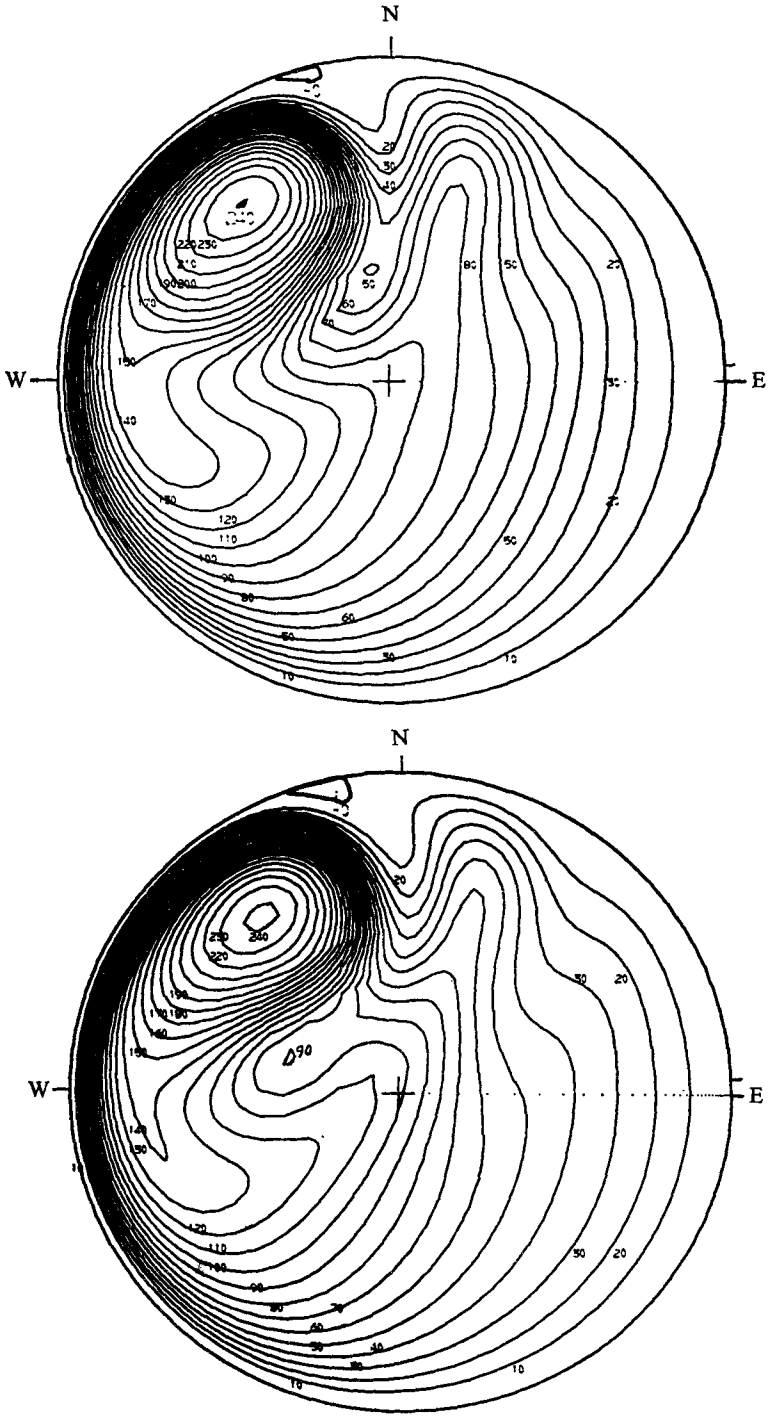

FIGURE 3. Contour plots of stream-function solution from a numerical experiment (N 13 in Beardsley 1973*b*) conducted in the unstable regime. (*a*), (*b*) are separated in time by $\Delta\tau = 0{\cdot}56\delta^{-1}$, approximately one-half the period of the instability. In (*b*) maximum value is 242; local minimum below it is 89.

strated in figure 2 (plates 1 and 2). Here the steady numerical stream functions for several representative values of $|\epsilon|/E^{\frac{1}{2}}$ have been superimposed on the corresponding laboratory streak photographs. (These composite photographs are taken from the original streak photographs of Beardsley (1973*b*, figures 6 (*a*), (*c*)) and Beardsley (1969, figure 11).) The location of the western boundary-layer vortex, the flow near the vortex, and the interior flow observed in both models is identical to within the basic accuracy of the laboratory measurements and photographic techniques. The principal difference between the flow patterns of the two models occurs in the transition region where the stationary topographic Rossby waves appear. The numerical model seems correctly to predict the Rossby wave wavelengths in figure 2, but slightly underestimates the wave amplitudes and slopes. Beardsley (1973*b*) gives a detailed analysis of the steady-state vorticity balance for the numerical solution shown in figure 2 (*c*), which indicates that direct Ekman-layer suction provides the dominant dissipative control in the boundary-layer vortex region, while both Ekman-layer suction and lateral friction become comparable to the driving term in (8) in the region of the damped standing topographic Rossby waves.

The steady flow in the numerical model becomes unstable when a critical value of $|\epsilon|$ is reached. After decay of the starting transients, the total kinetic energy exhibits moderate, slowly-growing periodic oscillations in time. This flow instability found in the numerical model is qualitatively identical with the low-frequency instability observed in the laboratory model. In both models, a small secondary vortex is formed periodically in the transition region to the east of the main boundary-layer vortex. This secondary vortex then decays as it is swept south-west by the primary vortex. The position of the secondary vortex is shown as a function of time in figures 3 (*a*), (*b*). These two stream-function plots are separated by $\Delta\tau = 0{\cdot}56\delta^{-1}$, which is approximately one-half the period of the instability for this case. These figures are very similar to the laboratory streak photograph of Beardsley (1969, figure 12) taken in the unstable regime.

Both laboratory and numerical experiments indicate that the onset of this instability depends critically on ϵ and E, but not on the bottom slope s. In the laboratory experiments, the transition to instability is defined by the curve

$$Re_c = |\epsilon|/E^{\frac{1}{2}} = 11{\cdot}3 \pm 0{\cdot}2 + (1{\cdot}26 \pm 0{\cdot}05) \times 10^5 E,$$

where Re_c is the critical value of the Reynolds number based on the external forcing and Ekman-layer scale thickness. The stability curve suggested by the numerical solutions exhibits the observed linear dependence of Re_c on E (as shown in figure 4), but indicates that a greater driving stress is required in the numerical model for instability. As will be evident, this is primarily due to the slight underestimation of the topographic Rossby wave amplitude and slope by the numerical model for identical external parameters. In terms of the parameters defined for the numerical model, the critical value of $Re = 2R_0\delta^{-2}$ depends linearly on $\hat{E}^2/\delta^2$.

S. Godfrey (1971, private communication) first suggested that the low frequency instability observed in the laboratory model could be generated by a *local* breakdown or instability of the topographic Rossby wave embedded in the western boundary current transition flow. The local character of the insta-

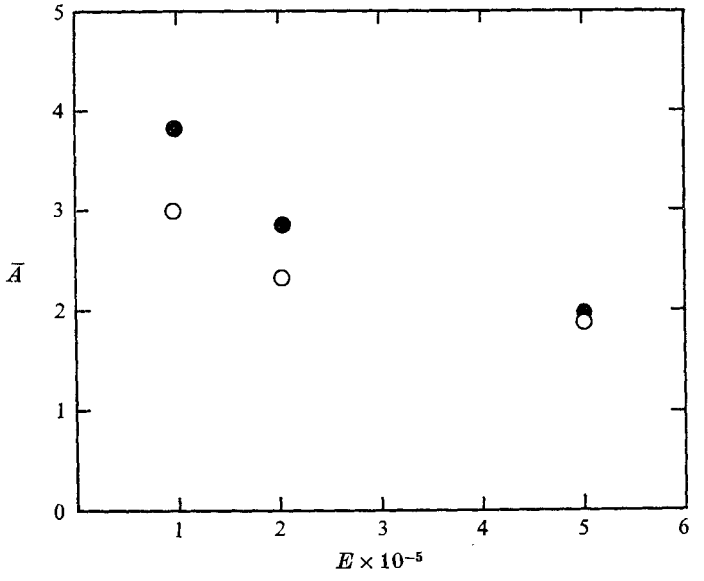

FIGURE 4. Comparison of the measured A_m (●) and the theoretical value A_t (○) predicted using (13) as a function of external Ekman number.

bility implies that the formation of the secondary vortex is not appreciably influenced by the presence of the boundaries. The onset of the instability is then determined by the local dynamics in the transition region, with the consequence that the isolated instability mechanism may be described analytically.

A qualitative description of this instability can be obtained through the study of the non-dimensional flow field

$$\psi_0 = \Gamma y + A \sin kx$$

as an approximation to the actual numerical solution in the transition region where the decaying topographic Rossby waves appear. Although ψ_0 does not satisfy the full viscous equations† or the boundary conditions in the circular basin, it closely resembles the actual numerical and laboratory flows in the region where the instability is initiated. To test the stability of the approximate solution, we shall study the perturbed flow

$$\psi = \psi_0 + \phi(x, y) \exp(i\sigma t),$$

where $\phi(x, y)$ satisfies the linearized version of the full model vorticity equation (8)

$$i\sigma\nabla^2\phi + R_0\{\psi_{0x}\nabla^2\phi_y - \psi_{0y}\nabla^2\phi_x - \nabla^2\psi_{0x}\phi_y\} + \phi_x = -\delta\nabla^2\phi + \hat{E}\nabla^4\phi. \quad (10)$$

† Actually, the expression $\Gamma y - \alpha x + A \exp(-\Delta x) \sin kx$ is an *exact* steady solution of the model vorticity equation (8), with $\alpha = 1$ and $\Delta \sim O(E^{\frac{1}{2}}k^2)$. Since breakdown is initiated in a small region ($x > 2\pi/k$) where the amplitude and wave slope are a maximum, we assume that the exponential eastward decay of the basic topographic wave field will not change the basic character of the instability, justifying the much simpler analysis of the approximate form of the basic flow ψ_0 given above.

A small initial disturbance $\phi(x, y)$ will grow when $\operatorname{Im}\sigma < 0$, and the criterion for marginal stability is $\operatorname{Im}\sigma = 0$.

The perturbation vorticity equation (10) is invariant under the transformation

$$x \to \frac{x'}{k}, \quad y \to \frac{y'}{k}, \quad \sigma \to \frac{\sigma'}{k}, \quad \delta \to \frac{\delta'}{k}, \quad \hat{E} \to \frac{\hat{E}'}{k^3},$$

$$R_0 \to \frac{\hat{R}'}{k^2}, \quad \psi_0 \to \frac{\psi_0'}{k}, \quad \phi \to \frac{\phi'}{k}, \quad A \to \frac{A'}{k}.$$

So the topographic Rossby wavenumber k can be scaled out of the problem. Substituting $\psi_0' = \Gamma y' + A' \sin x'$ into the scaled version of (10), and dropping primes, we find

$$i\sigma\nabla^2\phi + \hat{R}\{A\cos x[\nabla^2\phi_y + \phi_y] - \Gamma\nabla^2\phi_x\} + \phi_x = -\delta\nabla^2\phi + \hat{E}\nabla^4\phi. \tag{11}$$

The separation $\phi(x, y) = f(x)\exp(i\lambda y)$ can be made without loss of generality, because y does not appear explicitly in (11). Since our analysis is strictly confined to the breakdown region $0 < x < 1$, and ignores the weak spatial decay of the stationary topographic Rossby wave, we impose periodic boundary conditions on ϕ and expand $f(x)$ in a Fourier series. The substitution of

$$\phi = \exp(i\lambda y) f(x) = \exp(i\lambda y) \sum_{-\infty}^{\infty} f_n \exp(inx)$$

into the reduced vorticity equation (11) produces an infinite set of algebraic equations for the Fourier coefficients f_n:

$$\tfrac{1}{2}\lambda\hat{R}Ab_{n+1} f_{n+1} + ([i\tilde{\sigma} - i\omega]a_n + c_n) f_n + \tfrac{1}{2}\lambda\hat{R}Ab_{n-1} f_{n-1} = 0, \tag{12}$$

where

$$a_n = n^2 + \lambda^2, \quad b_n = n^2 + \lambda^2 - 1,$$

$$c_n = -in^2\hat{E}(n^2 + \lambda^2) + n(\theta n^2 + \theta\lambda^2 - 1),$$

$$i\tilde{\sigma} = \sigma, \quad \omega = \delta + \lambda^2\hat{E}, \quad \theta = -\Gamma\hat{R}.$$

This system has been examined in the inviscid limit $\delta = \hat{E} = 0$ by Lorenz (1972) in his study of the stability of a standing barotropic planetary wave. He showed, as did Godfrey, that the set can be solved by successive iteration, using a truncated expansion technique. The first approximation is obtained by setting all $f_n = 0$ for $|n| > 1$. The truncated set (12) then simplifies to

$$\begin{bmatrix} a_{-1}(i\tilde{\sigma} - i\omega) + c_{-1} & \tfrac{1}{2}\lambda\hat{R}Ab_0 & 0 \\ \tfrac{1}{2}\lambda\hat{R}Ab_{-1} & a_0(i\tilde{\sigma} - i\omega) & \tfrac{1}{2}\lambda\hat{R}Ab_1 \\ 0 & \tfrac{1}{2}\lambda\hat{R}Ab_0 & a_1(i\tilde{\sigma} - i\omega) + c_1 \end{bmatrix} \begin{bmatrix} f_1 \\ f_0 \\ f_1 \end{bmatrix} = 0, \tag{13}$$

which yields a cubic characteristic equation for $\tilde{\sigma}$ with real coefficients. Since the lowest transition to instability occurs at $\tilde{\sigma} = 0$, the criterion for marginal stability is

$$\gamma_c^2 = (\hat{R}A)^2 = \frac{2(1+\lambda^2)}{\lambda^2(1-\lambda^2)(\hat{E}+\omega)}\left[\omega^3 + 2\hat{E}\omega^2 + \omega\hat{E}^2 + \frac{\omega(\theta + \theta\lambda^2 - 1)^2}{(1+\lambda^2)^2}\right]. \tag{14}$$

The critical value of γ_c for a given set of external parameters is determined by minimizing (14) with respect to λ, the scaled north–south wavenumber of the perturbation. Truncation of the set (12) at second order (i.e. retaining only f_n for $|n| \leqslant 2$) changes the numerical values computed for γ_c by less than 1 % in the range of parameters relevant here.

The parameter γ_c is proportional to the maximum slope of the stationary finite-amplitude topographic Rossby wave; and (14) states that, for a given set of external parameters, the slope of the stationary wave must exceed the initial value indicated by γ_c for the flow to be unstable. This result indicates the definite constraint that dissipative mechanisms like 'lateral' and 'bottom' friction place on the basic instability mechanism. In their studies of the inviscid instability, both Lorenz (1972) and Gill (1974) found that a planetary wave held stationary on a uniform eastward current is *always* unstable with the temporal growth of the perturbation being proportional to the initial amplitude of the original wave. Here dissipative mechanisms tend to stabilize the basic flow. Note also from (14) that the north–south wavenumber of the perturbation eddy must be less than the wavenumber of the basic topographic Rossby wave for instability to occur. This is a consequence of the conservation of mean energy and mean-square vorticity (or enstrophy) for two-dimensional motion of an ideal fluid (see Longuet-Higgins & Gill 1967). When a primary wave loses energy, some of that lost energy must be transferred to a shorter, and some to a longer wave. In our truncated representation to first order $\exp(i\lambda\bar{y})\, f_0$ must correspond to the longer wave (hence $|\lambda| < 1$), while the shorter waves are given by $\exp i(\lambda\bar{y} \pm \bar{x})$.

One test of this stability analysis is to make a comparison between model and experiment, to see if the theory can accurately predict the onset of the instability in the laboratory or numerical model. Since the analysis is based on the vorticity equation used in the numerical study, we chose the results of the numerical model as the basis of comparison. Measurements of the principal parameters were made in the transition region from plots of the steady numerical solutions. The scaled radius of the circular boundary is unity and the standard contour interval for the plots of ψ is 0·1 (as in figure 2). The wavelength of the basic topographic Rossby wave is taken as the interval in the x direction between adjacent peaks (or local maximum extensions in y) along a single streamline in the transition region (again see figure 2). The parameter Γm was computed using the measured y increment Δy between three adjacent streamlines, and

$$\Gamma_m = \Delta\psi/\Delta y = -|0{\cdot}2/\Delta y|.$$

The observed scaled amplitude A_m of the stationary topographic Rossby wave was then determined from

$$A_m = \tfrac{1}{2}\Gamma_m \Delta y.$$

Δy is the vertical peak-to-valley distance on a single streamline through the transition region. Using the external parameters to evaluate $\hat{R}_{\exp}$, a theoretical value of the amplitude $A_t = \gamma_c/\hat{R}_{\exp}$ can be computed using (14). The observed A_m and theoretical A_t values, determined from the steady numerical solutions closest to the stability curve at the three different values of the Ekman number studied, are plotted in figure 4. The observed values A_m and the theoretical

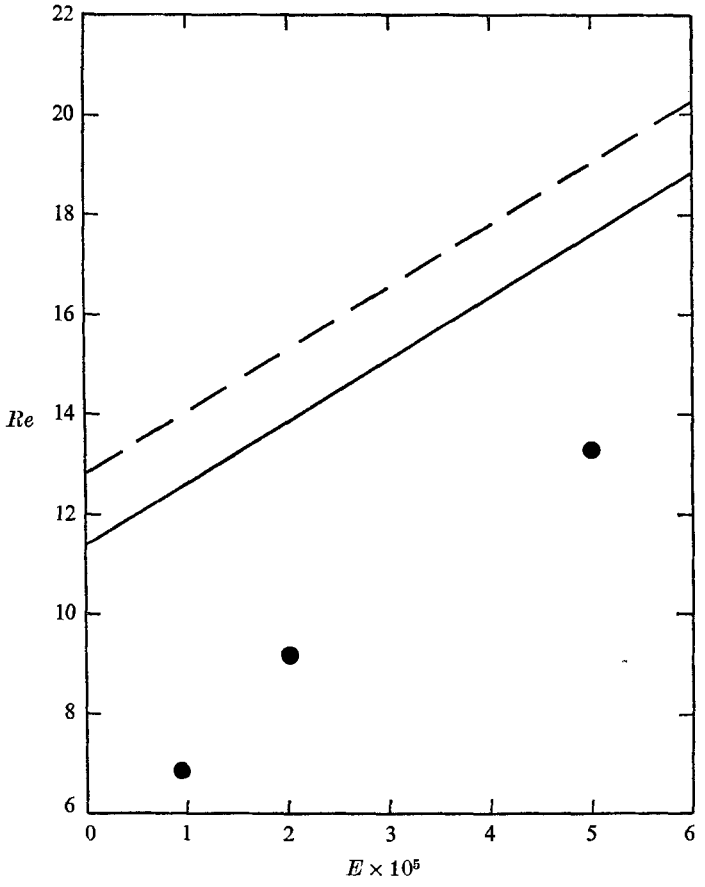

FIGURE 5. Stability diagram for steady forcing in the 'sliced cylinder' problem. ——, stability curves determined from laboratory experiments; – – –, those determined from numerical experiments; ●, values of Re_c predicted by analytic stability analysis.

values A_t exhibit a similar inverse dependency on E. An alternative approach is to compute the critical Reynolds number from

$$Re = \frac{2\hat{R}}{\delta^2} = \frac{2}{\delta^2}\left[\frac{\gamma_c}{A_m}\right].$$

Since $\gamma_c = \gamma_c(\theta, \hat{E}, \delta)$ and $\theta = -\Gamma\hat{R}$, we must solve the functional equation

$$\hat{R} = \gamma_c(\Gamma\hat{R}, \hat{E}, \delta)/A_m,$$

to obtain an estimate of $\hat{R}$. The values of Re calculated by this method are shown in figure 5 for the three numerical experiments closest to marginal stability. The three computed values of Re form an approximately straight stability curve, parallel to but below the experimentally determined curves. Since viscosity plays a stabilizing role in this stability mechanism, we should expect the critical Reynolds number to be higher if the full viscous problem were treated. If the basic solution ψ_0 is modified to balance the forcing in the basic vorticity equation

(i.e. $\psi_0 = \Gamma y - bx + A\sin x$), the same analysis holds, except that $i\tilde{\sigma} = \tilde{\sigma} - \lambda b\hat{R}$ in (12). When $\tilde{\sigma} = 0$, the actual scaled frequency $\sigma = \lambda b\hat{R}$, and

$$\phi(x,y) = f(x)\exp i\lambda(y + b\hat{R}t),$$

indicating that the perturbation field is swept southward (in agreement with laboratory and numerical observations). The quantity b/Γ is the average slope of a streamline; it can be measured from the numerical contour plots. The basic period of the instability can then be estimated as the time it takes for a wave with phase speed $b\hat{R}$ to traverse half the tank. The results confirm the tendency of the observed period to decrease with increasing external Ekman number.

In summary, a simple analytic model has been presented, which attempts to interpret the onset of the low-frequency instability observed in both laboratory and numerical sliced-cylinder models, in terms of a local breakdown of the stationary topographic Rossby wave trapped in the downstream transition region of the western boundary current. In view of the approximate nature of the instability model, and the fitting of this model to the much more complicated flows observed in the sliced-cylinder problem, the theoretical model shows surprisingly good agreement with the experimental results, and thus substantiates the *local* nature of the breakdown. The analysis also indicates that this instability mechanism is not peculiar to the sliced-cylinder geometry but is an intrinsic feature of β-plane flows. Dissipative processes in the sliced-cylinder problem (namely lateral and bottom friction) inhibit the onset of the instability, until the wave slope exceeds a finite critical value. The basic mechanism here is really the *inviscid* mechanism examined independently by Godfrey and Lorenz (1972). The nature of the inviscid instability has been further clarified by Gill (1974), who found that two parameters govern the stability of a barotropic planetary wave on an infinite β plane (namely, the direction of the wavenumber of the planetary wave and the local Rossby number $M = uk^2/\beta$: u is the velocity amplitude of the wave, k its wavenumber). For large M, inertial effects dominate β effects, and the mechanism is like the Rayleigh inflexion-point instability for two-dimensional shear flow. In the limit $M \to 0$, the instability mechanism may be described in terms of weak resonant wave interaction theory. In the sliced-cylinder results discussed here, the local Rossby number defined by Gill for the primary wave is simply

$$M = \frac{\epsilon E^{\frac{1}{2}}}{2s^2}\left(\frac{\partial \Psi}{\partial y}k^2\right) = R_0\left(\frac{\partial \psi}{\partial y}\right)k^2.$$

The actual value of M for those numerical experiments near the stability curve is approximately 5, indicating by Gill's criterion that, while β effects are still important, the instability mechanism observed in the sliced-cylinder results is more like a Rayleigh instability.

As pointed out by Gill (1974) and others, there is growing evidence that the β and inertial effects are comparable in the dominant meso-scale eddies, so that $M = O(1)$ is the relevant range to examine for oceanic phenomena. While other (especially baroclinic) processes must also influence the dynamics of major currents and eddies in the ocean, we have extended the inviscid analysis of the stability of a baratropic planetary wave to include weak frictional effects. We

have then used this analysis to explain the low-frequency instability observed in the sliced-cylinder model for the wind-driven ocean circulation. The sliced-cylinder model was originally introduced by Pedlosky & Greenspan (1967), because of the similarity of the model flow in the linear regime with large-scale ocean circulation. We have seen here that, even in the nonlinear regime, this model has produced geophysically interesting flows to study, including the breakdown of finite-amplitude planetary waves.

The authors would like to acknowledge the initial suggestion for the stability analysis kindly given by Dr S. Godfrey. We also wish to thank Dr A. Gill for sending us an early manuscript on his analysis. Mrs B. Wysochansky and Mr S. Ricci assisted in the preparation of the manuscript and figures. We also wish to acknowledge the Mathematical Laboratory Group of Project MAC at MIT for the use of their computer system in some of the stability computations. This research was supported by the Office of Naval Research (N00014-67-A-0204-0048) and the National Science Foundation (grants GA-41073 and GA-41075).

REFERENCES

BEARDSLEY, R. C. 1969 A laboratory model of the wind-driven ocean circulation. *J. Fluid Mech.* **38**, 255.

BEARDSLEY, R. C. 1973*a* A numerical model of the wind-driven ocean circulation in a circular basin. *Geophys. Fluid Dyn.* **4**, 211.

BEARDSLEY, R. C. 1973*b* A numerical investigation of a laboratory analogy of the wind-driven ocean circulation. *Proc.* 1972 *NAS Symp. on Numerical Models of Ocean Circulation.*

BRYAN, K. 1963 A numerical investigation of a nonlinear model of a wind-driven ocean. *J. Atmos. Sci.* **20**, 596.

GILL, A. 1974 Stability of planetary waves. *Geophys. Fluid Dyn.* **6**, 29.

GREENSPAN, H. P. 1968 *The Theory of Rotating Fluids.* Cambridge University Press.

GREENSPAN, H. P. 1969 A note on the laboratory simulation of planetary flows. *Studies in Appl. Math.* **48**, 147.

ISRAELI, M. 1970 A fast implicit numerical method for time dependent viscous flows. *Studies in Appl. Math.*, **49**, 327.

LONGUET-HIGGINS, M. S. & GILL, A. E. 1967 Resonant interactions between planetary waves. *Proc. Roy. Soc.* A **299**, 120–140.

LORENZ, E. N. 1972 Barotropic instability of Rossby wave motion. *J. Atmos. Sci.* **29**, 258.

MUNK, W. H. 1950 On the wind-driven ocean circulation. *J. Meteor.* **7**, 79–93.

ORSZAG, S. & ISRAELI, M. 1972 Numerical flow simulation by spectral methods. *Proc.* 1972 *NAS Symp. on Numerical Models of Ocean Circulation.*

PEARSON, C. E. 1965 A computational method for viscous flow problems. *J. Fluid Mech.* **21**, 611.

PEDLOSKY, J. & GREENSPAN, H. P. 1967 A simple laboratory model for the oceanic circulation. *J. Fluid Mech.* **27**, 291.

STOMMEL, H. 1948 The westward intensification of wind-driven ocean currents. *Trans. Am. Geophys. Un.* **29**, 202.

SVERDRUP, H. 1947 Wind-driven currents in a baroclinic ocean. *Proc. Nat. Acad. Sci.* **33**, 318.